





## Singular behavior of microfluidic pulsatile flow due to dynamic curving of air-fluid interfaces

Pamela Vazquez-Vergara <sup>1,2</sup> Ulises Torres-Herrera <sup>1</sup> Luis F. Olguin <sup>2</sup>  
and Eugenia Corvera Poiré <sup>1,3,\*</sup>

<sup>1</sup>*Departamento de Física y Química Teórica, Facultad de Química, Universidad Nacional Autónoma de México, 04510 Ciudad de México, Mexico*

<sup>2</sup>*Laboratorio de Biofisicoquímica, Facultad de Química, Universidad Nacional Autónoma de México, 04510 Ciudad de México, Mexico*

<sup>3</sup>*UBICS Institute of Complex Systems, Universitat de Barcelona, Martí i Franquès 1, 08028 Barcelona, Spain*



(Received 23 October 2020; accepted 13 January 2021; published 10 February 2021)

Pulsatile pressure gradients are widely present in microfluidic multiphase systems where the movement of fluids is affected by the presence of fluid-fluid interfaces. We present a simple theoretical model that incorporates dynamic interfacial curvatures produced as a response to pulsatile external forcing. Our equations make evident a singular character of the dynamics at low frequencies, due to surface tension. Analytical solution of the model shows the emergence of a resonant behavior for the dynamic permeability. We have designed and implemented microfluidic experiments to observe both the low-frequency dynamics and the resonance. We have studied a fluid slug whose length was chosen in order to look for resonances as predicted by our theoretical model, in the range of operational frequencies of our piezoelectric actuator. We have obtained the experimental dynamic permeability for water and a 70.0% glycerol solution in water and observed agreement with theoretical findings. Our model, validated by experiments, allows us to understand differences of several orders of magnitude in the amplitude of flow velocity at low frequencies, between systems with and without interfaces.

DOI: [10.1103/PhysRevFluids.6.024003](https://doi.org/10.1103/PhysRevFluids.6.024003)

### I. INTRODUCTION

Pulsatile flow in microfluidics has many applications. It has been employed to increase the efficiency of liquid-liquid extraction of organic compounds [1,2], promote the mixture of parallel water streams [3,4], align anisotropic particles [5], study DNA elongation [6,7], and carry out chemical reactions in multiphase flow [8]. Pulsatile flow in microfluidics is often present unintentionally in microdevices containing drops since these ones create an oscillatory dynamics of the pressure drop [9], not only in channels conveying drops, but in channels connected to them [10].

The characterization of a fluid response to a pulsatile pressure gradient has often been described, both theoretically and experimentally, by the dynamic permeability, which constitutes a frequency-dependent linear response of a fluid to a dynamic pressure gradient. Knowledge of the dynamic permeability allows one to know the amplitude of the velocity caused by each of the frequency modes, involved in the pressure gradient [11–21].

An intrinsic feature of the dynamic permeability for Newtonian fluids in rigid channels is a monotonic decay with frequency [11,19]. In a log-log scale, this distinct behavior shows a plateau at frequencies below the viscous frequency, and a decay, as the inverse of frequency, for frequencies

---

\* Author to whom correspondence should be addressed: [eugenia.corvera@gmail.com](mailto:eugenia.corvera@gmail.com)

higher than the viscous one. The dynamic permeability has also been obtained theoretically for Newtonian fluids in elastic tubes where a resonant behavior at frequencies in the range of ultrasound emerges for fluids confined in elastomeric materials at microscales [22,23]. This radically different behavior seems to emerge whenever there is an element in the system that allows for bouncing of pressure waves, be it an elastic wall [22], a viscoelastic fluid [16,19,20], or a branching structure [24]. The formalism of the dynamic permeability has also been used to describe compressible Newtonian binary fluids, with negligible capillary effect, and a resonance has been found whenever the compressibility of the lowest viscosity fluid is relevant [25].

Experimentally, the dynamic permeability has been obtained only at macroscales [19,20]. This has been done by driving the fluids with oscillatory pressure gradients, and tracking tracer particles with laser Doppler anemometry (LDA) and particle image velocimetry (PIV) techniques. Experimental resonances in the dynamic permeability have not been reported at microscales. At these scales, knowing this response would be particularly pertinent, since fluids are generally in the linear regime. Observing resonances at such small scales is challenging, since the resonance frequency scales as the inverse of some power of the smallest dimension in the system [16,17,22,25,26], so, a fine tuning between density, viscosity, elastic times, and confining scales is decisive to find resonances at frequencies that could be experimentally imposed and recorded. Also, at microscales  $\mu$ PIV techniques need a sophisticated setup [27]. Furthermore, at microscales, techniques used at macroscales would have restrictions related to visualization [28,29].

The dynamic permeability at microscales, for Newtonian fluids that are in contact with elastic media like cells, interfaces, elastic walls, or several of them, is expected to have a nonmonotonic behavior as a function of frequency at certain conditions. This feature, if experimentally confirmed, could be potentially exploited for organ-on-a-chip experiments to recreate the physiological mechanical conditions of the cells of a particular organ [30–33], since most of natural processes occur at certain characteristic frequencies, or to study how cells would respond to different imposed, nonphysiological, external stresses [34–36].

In this work, we consider the pulsatile dynamics of a Newtonian fluid slug containing two air-fluid interfaces. We develop the simplest theoretical model for which the shape of the interfaces is a response to the external forcing, by considering that the pressure of the fluid at interfaces is affected by Laplace condition, that dynamically modifies the pressure in proportion to the local curvature. We have also designed and implemented a microfluidic experiment to study the pulsatile dynamics of Newtonian fluids in the presence of interfaces. Our method for interface tracking is simple and straightforward (it needs only a microscope and a high-speed camera). We also use a pressure sensor to record the pressure drop at both sides of the fluid slug. We have characterized the behavior of water and a 70.0% glycerol solution in water, as model fluids. We have used the vibrations of a piezoelectric crystal to move the fluid slug, back and forth, within the microchannel. The experimental setup is illustrated in Fig. 1. We have found that the presence of surface tension confers a radically different behavior to the dynamic permeability, not only when compared with the one of a single fluid, but when compared to the one of any other system reported in the literature, including those having elastic features. We have found an agreement between the experimentally determined dynamic permeability and our theoretical model, which predicts a singular behavior, with an associated monotonic increase at low frequencies, due to the presence of surface tension.

## II. MODEL

We consider a fluid slug of length  $L$  containing two fluid-air interfaces that flows on the  $x$  direction of a rectangular microchannel whose velocity at the confining plates (in  $z = \pm\ell$ ) vanishes. The separation between these plates,  $2\ell$ , gives the microchannel thickness. A diagram of the system's geometry is shown in Fig. 2.

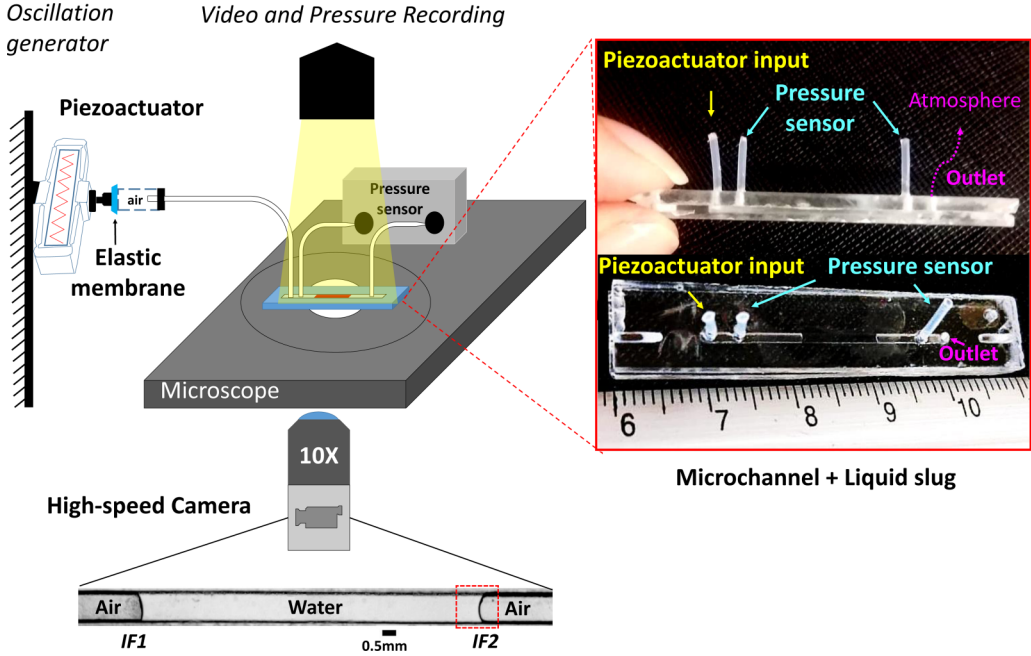


FIG. 1. Experimental setup. The oscillations are generated by the periodic movement of a piezoelectric actuator that moves back and forth a liquid slug confined within the microchannel via moving the air trapped between the piezoactuator and the slug. The pressure drop dynamics is registered at both sides of the fluid slug. A high-speed video camera records the interface movement.

The driving force of the system is a pressure drop, external to the fluid slug,  $\Delta p_{\text{air}}$ , that can vary in time. The linearized Navier-Stokes equation for the fluid is

$$\rho \frac{\partial v}{\partial t} = -\frac{\Delta p_{\text{fluid}}}{L} + \eta \frac{\partial^2 v}{\partial z^2}. \quad (1)$$

For the equation,  $\Delta p_{\text{fluid}}$  is the pressure drop inside the fluid slug,  $v$  is the fluid velocity, and  $\eta$  and  $\rho$  are respectively the viscosity and density of the fluid forming the slug.

According to Laplace condition, the presence of interfaces, located at the left and right sides of the fluid slug, modify the pressure drop in such a way that

$$\Delta p_{\text{fluid}} = \Delta p_{\text{air}} + \sigma \kappa_1 + \sigma \kappa_2, \quad (2)$$

where  $\sigma$  is the surface tension between fluid and air, and  $\kappa_1$  and  $\kappa_2$  are the instantaneous interfacial curvatures on the left and right sides of the fluid slug, respectively [37]. For neutral wetting, these

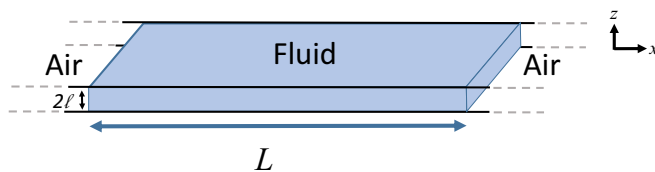


FIG. 2. System's geometry showing a fluid slug consisting of a volume of fluid and two air-fluid interfaces. The slug has length  $L$ , and it is confined between rectangular plates separated by a distance  $2l$ . The fluid displacement occurs in the  $x$  direction. Details can be found in Appendix A.

would be zero in the absence of forcing and would be different from zero in the presence of an external forcing.

The shapes of the interfaces are, respectively,  $u_1(z, t)$  and  $u_2(z, t)$ . For small driving forces, curvatures can be approximated as concavities of the interface; the equation for the fluid would then read

$$\rho \frac{\partial v}{\partial t} = -\frac{\Delta p_{\text{air}}}{L} + \eta \frac{\partial^2 v}{\partial z^2} + \frac{\sigma}{L} \frac{\partial^2 u_1}{\partial z^2} + \frac{\sigma}{L} \frac{\partial^2 u_2}{\partial z^2}. \quad (3)$$

Continuity at the interface requires velocities of fluid and interface to be equal, that is,

$$\frac{\partial u_1}{\partial t} = \frac{\partial u_2}{\partial t} = v(z, t), \quad (4)$$

where we have considered that variations of velocity in the  $x$  direction are much smaller than its variations in between the confining plates. Substitution of Eq. (4) into Eq. (3) gives an integro-differential equation, in space and time, for the fluid velocity  $v(z, t)$ ,

$$\rho \frac{\partial v}{\partial t} = -\frac{\Delta p_{\text{air}}}{L} + \eta \frac{\partial^2 v}{\partial z^2} + \frac{2\sigma}{L} \frac{\partial^2}{\partial z^2} \int v dt. \quad (5)$$

This is our model equation for the velocity of a fluid slug containing two interfaces. The integral character of Eq. (5) in the time domain is easy to handle if this is transformed to frequency domain, namely

$$-i\rho\omega\hat{v} = -\frac{\Delta\hat{p}_{\text{air}}}{L} + \left[ \eta + i\frac{2\sigma}{L\omega} \right] \frac{\partial^2 \hat{v}}{\partial z^2}. \quad (6)$$

Equation (6) shows that surface tension causes an effectively complex viscosity, analogous to the one characterizing a viscoelastic fluid. This is due to the elastic nature of surface tension. However, the imaginary part of this complex viscosity diverges in the limit of small frequencies, a behavior that is not as in models of viscoelastic fluids, where the imaginary part of the complex viscosity vanishes. At low frequencies, the capillary term will be more important than the viscous one, and we expect a totally different behavior for the low-frequency dynamics of the fluid, than in the absence of surface tension. Solution of Eq. (6) in the frequency domain, subject to no-slip boundary conditions, gives

$$\hat{v}(z, \omega) = -\frac{K_L(z, \omega)}{\eta} \frac{\Delta\hat{p}_{\text{air}}}{L}, \quad (7)$$

where the complex local dynamic response function,  $K_L(z, \omega)$ , that we call local dynamic permeability, is given by

$$K_L(z, \omega) = -\frac{\eta}{i\omega\rho} \left[ 1 - \frac{\cos(Az)}{\cos(Al)} \right], \quad (8)$$

with  $A^2 \equiv \frac{i\omega\rho}{\eta[1+i\frac{2\sigma}{L\eta\omega}]}$ . For the velocity, averaged over the cross-sectional area of the microchannel, we have

$$\langle \hat{v}(\omega) \rangle = -\frac{K_G(\omega)}{\eta} \frac{\Delta\hat{p}_{\text{air}}}{L}, \quad (9)$$

where the complex global dynamic response,  $K_G(\omega)$ , that we call global dynamic permeability, is given by

$$K_G(\omega) = -\frac{\eta}{i\omega\rho} \left[ 1 - \frac{\sin(Al)}{Al \cos(Al)} \right]. \quad (10)$$

Equations (7) and (8) give the velocity profiles, while Eq. (9) and Eq. (10) give a generalized Darcy's law for the velocity of the fluid slug, averaged over the cross-sectional area. Equations (8)

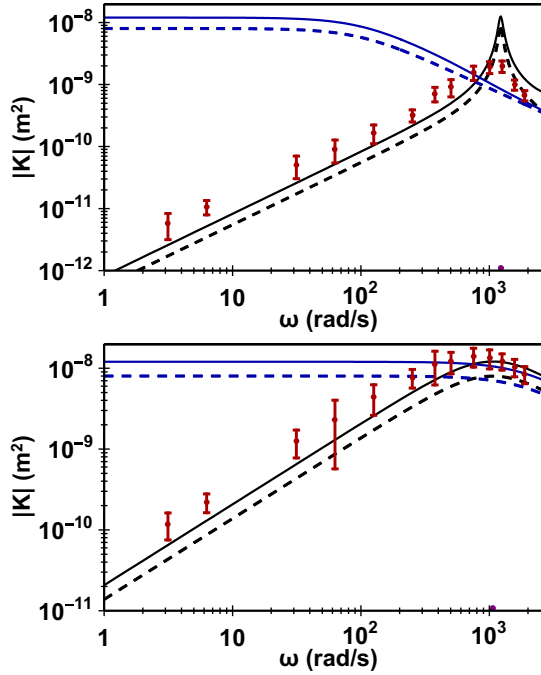


FIG. 3. Comparison of the local dynamic permeability,  $K_L$ , with continuous lines, for water (top panel) and 70.0% glycerol solution in water (bottom panel) in the absence of interfaces (blue) and for a slug containing two air-fluid interfaces (black). Dashed lines denote the corresponding global permeabilities,  $K_G$ . Theoretical parameters used correspond to a slug of water of 1 cm length, confined between rectangular plates, separated by a distance of  $310 \mu\text{m}$ . For water (top panel) fluid parameters are surface tension  $73 \text{ mN/m}$ , density  $997 \text{ kg/m}^3$ , and viscosity  $0.001 \text{ Pa}\cdot\text{s}$ . For 70.0% glycerol solution in water (bottom panel) fluid parameters are surface tension  $65.26 \text{ mN/m}$ , density  $1181.25 \text{ kg/m}^3$ , and viscosity  $0.0225 \text{ Pa}\cdot\text{s}$ . Red dots correspond to experimental data; as explained in Sec. III, they should be compared with theoretical continuous black lines. The small dots in the horizontal axis indicate the resonance frequency predicted by the model.

and (10) are response functions to an external pressure drop,  $\Delta p_{\text{air}}$ , that determine the amplitude of local and global velocities, respectively, to each of the frequencies involved in the pressure drop.

Equation (8), evaluated in the middle of the microchannel (at  $z = 0$ ), and Eq. (10) have a similar mathematical behavior. This behavior is shown in the continuous and dashed black lines of Fig. 3. The leading term of the magnitude of the local dynamic permeability, at low frequencies, is given by  $\frac{|K_L|}{\eta} = \frac{Ll^2}{4\sigma}\omega$ , while the equivalent amount for the global permeability is given by  $\frac{|K_G|}{\eta} = \frac{Ll^2}{6\sigma}\omega$ . This allows us to write the local magnitude of the permeability in terms of the global one as  $|K_L| = \frac{3}{2}|K_G|$ , which explains the difference by a factor of  $\frac{3}{2}$  observed in a wide range of frequencies in Fig. 3. The figure also illustrates that the resonance frequency is the same for the local and global dynamic permeabilities. So, this should be determined by the term  $\frac{1}{\cos(Al)}$  present in both Eq. (8) and Eq. (10). These properties give experimental freedom on whether to measure local velocities or global flow rates.

The monotonically increasing behavior of the dynamic permeabilities at low frequencies is in clear contrast to the one for a single fluid in a rigid microchannel, characterized by a plateau at low frequencies, shown for reference in Fig. 3 with continuous and dashed blue lines. Regardless of how large the fluid slug is, a finite surface tension will force the magnitude of the global and local dynamic permeabilities to be zero in the zero-frequency limit. This has remarkable consequences for the fluid behavior at low frequencies; for example, our model says that, for the parameters for

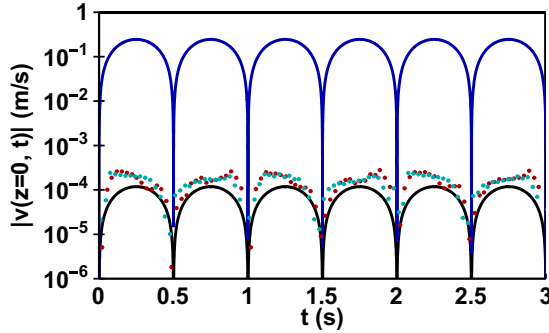


FIG. 4. Comparison of the theoretical magnitude of water velocity as a function of time, in the absence of interfaces (blue curve), where  $\sigma = 0$  and for a fluid slug containing two interfaces (black curve). Curves are obtained from Eqs. (14) and (8). Experimental data (red and cyan dots) are for two independent experiments for a water slug with pressure drop frequency of 1.0 Hz and pressure drop amplitude  $\Delta p_{\text{air}}^o = 204.0$  Pa.

water and 70.0% glycerol solution in water, used to compute Fig. 3 (top and bottom, respectively), the presence of two interfaces would reduce the magnitude of the permeability at a pulsating frequency of 1.0 Hz by over three and two orders of magnitude, respectively. This implies that for a given amplitude of the pulsatile pressure drop, the amplitude of the fluid velocity, in the presence of interfaces, has an enormous change with respect to the case of no interfaces present. This is illustrated in Fig. 4 with blue and black continuous lines, respectively, for water pulsed at 1.0 Hz. A log scale has been used for the magnitude of fluid velocity, in order to show the 3 orders of magnitude difference predicted, at this frequency, with and without interfaces.

A consequence of the monotonic increase at low frequencies caused by surface tension is that the dynamic permeability presents a resonance for Newtonian fluids. That is, there is a range of frequencies for which the magnitude of the local dynamic permeability (or its global version) increases as a function of frequency, due to the effect of surface tension, followed by a range of frequencies for which it will have the classical monotonic decay with frequency, due to viscosity. For intermediate frequencies in between these behaviors, there is a resonance. To rationalize this, we can write the argument  $A^2 l^2$ , entering trigonometric functions in Eqs. (8) and (10), as a function of two characteristic frequencies, namely,

$$\omega_\eta = \frac{\eta}{\rho l^2} \quad \text{and} \quad \omega_\sigma = \frac{2\sigma}{L\eta}, \quad (11)$$

as

$$A^2 l^2 \equiv \frac{i\omega}{\omega_\eta \left[ 1 + i \frac{\omega_\sigma}{\omega} \right]}. \quad (12)$$

We can see that for frequencies  $\omega$ , much larger than the characteristic frequency  $\omega_\sigma$ , the second term in squared brackets is irrelevant, and we recover the results for a single fluid, namely,  $A^2 l^2 = \frac{i\omega}{\omega_\eta}$ , for which Eqs. (8) and (10) have the well known, monotonic decay with frequency. On the other hand, for frequencies  $\omega$ , much smaller than the characteristic frequency  $\omega_\sigma$ , the second term in squared brackets dominates the first one, and we obtain  $A^2 l^2 = \frac{\omega^2}{\omega_\eta \omega_\sigma}$ , which becomes real, and gives the monotonic increase of Eqs. (8) and (10) as a function of  $\omega$ .

The resonance frequency obtained from our theoretical model is given, in terms of the two characteristic frequencies of the system, in Eq. (11), by

$$\omega_{\text{res}} = \frac{\pi}{2} \sqrt{\omega_\eta \omega_\sigma}, \quad (13)$$

that can also be written as  $\omega_{\text{res}} = \frac{\pi}{2} \sqrt{\frac{2\sigma}{\rho l^2 L}}$ . This expression allows us to see two important features of  $\omega_{\text{res}}$ , namely, it is independent of viscosity, and it reveals that the length of the fluid slug,  $L$ , could serve as a control parameter to tune the resonance—for a given fluid in contact with air, and a given channel geometry. It is important to see that it is the value of surface tension, the geometry of the channel and the length of the fluid slug that will determine the resonance frequency. For frequencies much larger than  $\omega_\sigma$  and  $\omega_{\text{res}}$ , the behavior of both the local and global dynamic permeabilities is as the one of a single fluid.

In order to compare theory with experimental results, we solve Eqs. (7) and (8) for a single-mode time-dependent pressure drop, with frequency  $\omega_0$  and amplitude  $\Delta p_{\text{air}}^o$ , namely,  $\Delta p_{\text{air}}(t) = \Delta p_{\text{air}}^o \cos(\omega_0 t)$ . Velocity profiles in the time domain are given by

$$v(z, t) = -\frac{1}{\eta} |K_L(z, \omega_0)| \cos[\phi(z, \omega_0) - \omega_0 t] \frac{\Delta p_{\text{air}}^o}{L}, \quad (14)$$

where  $|K_L(z, \omega_0)|$  and  $\phi(z, \omega_0)$  are the modulus and argument of the complex local dynamic permeability at the frequency imposed by the pressure drop. Note that  $\phi(\omega_0)$  determines also the phase difference between flow velocity and pressure drop. Since the cosine oscillates between  $-1$  and  $1$ , the amplitude of the local velocity at a given  $z$ ,  $v_{\text{max}}(z)$ , is obtained as  $v_{\text{max}}(z) = \frac{1}{\eta} |K_L(z, \omega_0)| \frac{\Delta p_{\text{air}}^o}{L}$ , which gives us a way to determine the local permeability in the middle of the channel, from experimental measurements of the amplitude of the velocity at the channel center,  $v_{\text{max}}(z = 0)$ , and measurement of the pressure drop amplitude outside the fluid slug,  $\Delta p_{\text{air}}^o$ , as

$$\frac{|K_L(0, \omega_0)|}{\eta} = \frac{v_{\text{max}}(z = 0)L}{\Delta p_{\text{air}}^o}. \quad (15)$$

In terms of nondimensional numbers, we can write a general relation at resonance in terms of Womersley,  $\text{Wo}^2 = \frac{\omega_0}{\omega_\eta}$ , and Laplace,  $\text{La} = 2\sigma\rho l/\eta^2$ , numbers, as follows:

$$\text{Wo}_{\text{res}}^2 = \frac{\pi}{2} \sqrt{\frac{l}{L}} \text{La}. \quad (16)$$

### III. EXPERIMENTS

We designed an experiment to study the pulsatile dynamics of Newtonian fluids in the presence of air-fluid interfaces. As a proof of concept, we used water (filtrated and deionized) and 70.0% glycerol solution in water (filtrated and deionized) as model fluids. We placed a relatively large fluid slug in a rectangular microchannel and used the vibrations of a piezoelectric actuator, mediated by air, to move the fluid slug, back and forth, within the microchannel. The experimental setup is illustrated in Fig. 1 (see Appendix A for details). The length of the fluid slug was chosen in order to look for resonances as predicted by our theoretical model, in the range of frequencies that our piezoelectric could vibrate.

For all of the experiments, the pressure difference in the air, at both sides of the fluid slug,  $\Delta p_{\text{air}}(t)$ , was recorded, and the central point of the interface position near the exit open to the atmosphere,  $U(t) = u_2(z = 0, t)$  (IF2, Fig. 1), was tracked during at least 15.0 oscillation cycles, using a high-speed camera. We illustrate this in the top and middle rows of Fig. 5 (left column) for 5.0 of these cycles. We observed that both signals follow a quasisinusoidal movement. To verify that their frequencies were the same as the frequency imposed by the oscillation generator, the time signals were transformed to the Fourier domain. Results for  $|\Delta \hat{p}_{\text{air}}|$  and  $|\hat{U}|$  are shown in the top and middle rows of Fig. 5 (right column), respectively. In all cases, the dominant peak coincided with the corresponding frequency imposed by the piezoelectric. Before computing the interface velocity, the curves for position versus time were smoothed. The instantaneous interface velocity,  $V(t) = v(z = 0, t)$ , was then obtained by differentiating numerically the curve of position vs time with a simple Euler method. An example of this is shown in the bottom row of Fig. 5 (left column).



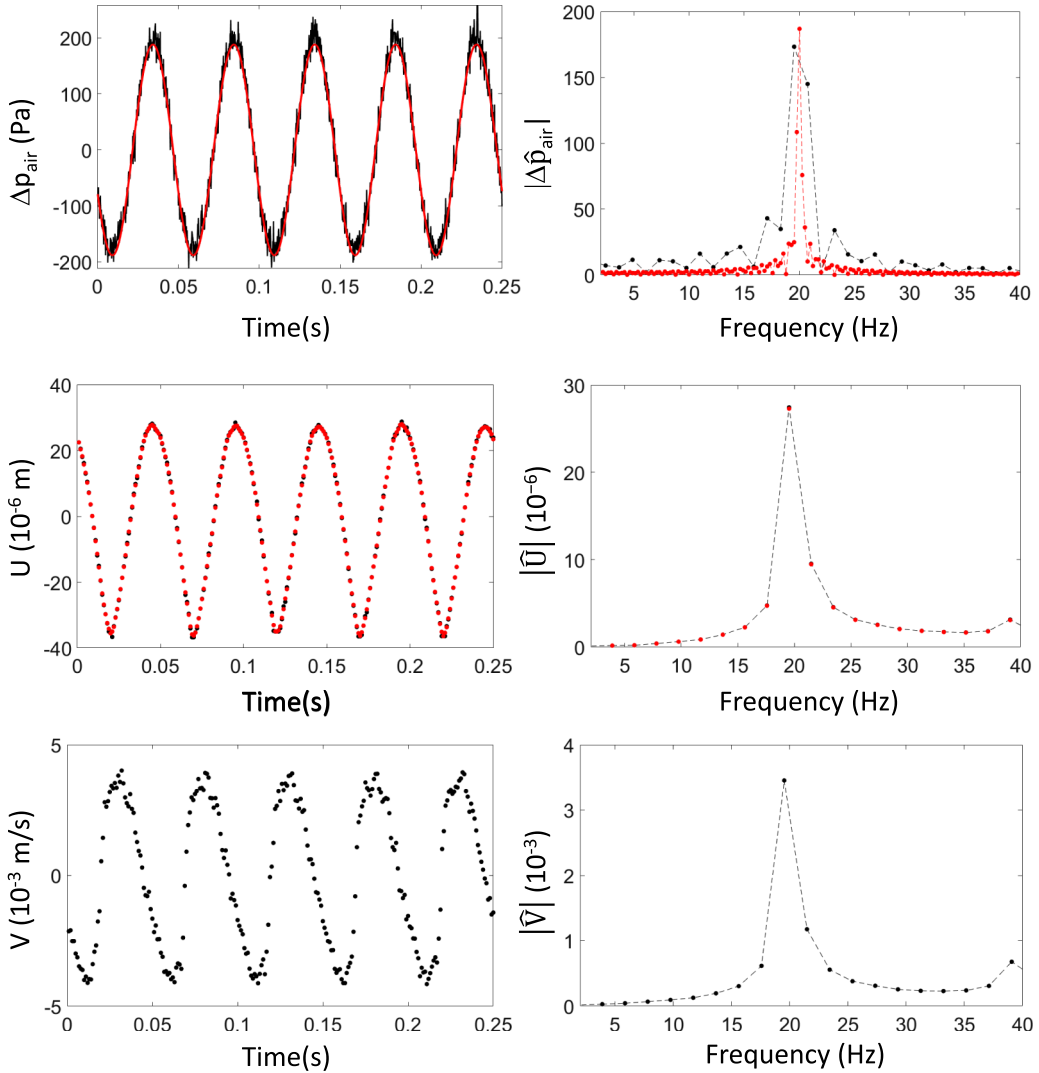


FIG. 5. Left column: Example of pressure drop, position, and interface velocity data, as a function of time, for a water slug driven periodically in the microfluidic channel. Pressure data were acquired at a sampling rate of 5000 data per second (black line) and fitted to a sine function (red line). Details are described in Appendix C. In the position versus time graph, raw experimental data points are shown in black; in red are the smoothed data obtained by using a moving average filter window of size four. The instantaneous interface velocity was obtained by differentiating numerically the smoothed curve of position vs time. Right column: Frequency spectra of the signals in the left column, showing a single dominant mode. Dashed lines are a guide to the eye. For position spectra, raw and smoothed signals overlap. For this example, a slug of water is oscillating at 20.0 Hz.

The spectra of the interface velocity also showed a dominant peak for  $|\hat{V}|$ , with the same frequency as in the Fourier domain, as shown in bottom row of Fig. 5 (right column).

The mean amplitude of the velocity,  $v_{\text{max}}$ , for each frequency was obtained by averaging the total number of maxima and minima for all the experiments, as explained in Appendix C. We then use Eq. (15) to experimentally determine the permeability,  $K_L = |K_L(0, 2\pi\nu_0)|$ . Figure 6 shows



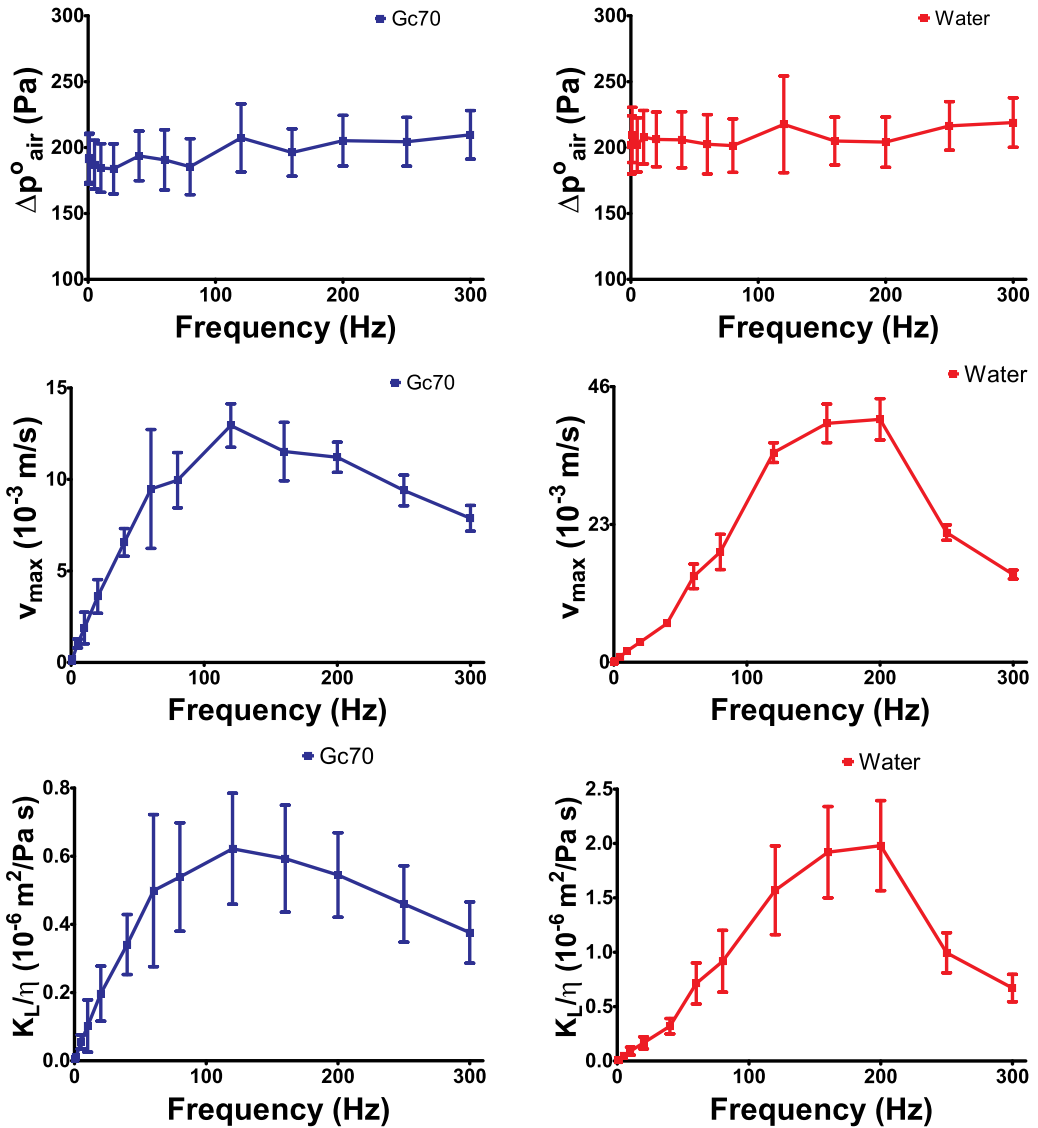


FIG. 6. Experimental amplitudes of pressure drop (top row), velocity (middle row), and permeability (bottom row), computed from experimental data, for 70.0% glycerol solution in water (left column) and water (right column). Solid lines are a guide to the eye.

our experimental results for the amplitude of the imposed pressure drop,  $\Delta p_{\text{air}}^{\circ}$ , the amplitude of velocity at the center of the microchannel,  $v_{\text{max}}$ , and the experimentally determined local dynamic permeability,  $K_L$ , as a function of the imposed frequency, in a linear scale. This scale allows for a detailed inspection of data and error bars. As the top row in Fig. 6 shows for 70.0% glycerol solution in water (left) and water (right), our method was able to impose an almost constant pressure drop amplitude of around 200 Pa for all the frequencies studied. This value for pressure drop was chosen as small as possible to allow for comparison with our linear theory, and large enough to allow for visualization and data processing of the interface movement.

The amplitude of the velocity is shown in middle row of Fig. 6 for 70.0% glycerol solution in water (left) and water (right). As expected from having imposed an almost constant amplitude for

the pressure drop, flow velocity has a behavior similar to the one expected for the permeability. However, when the permeability is computed, the small differences in pressure drop for different frequencies are compensated to give the proper response for any pressure drop in the linear regime.

Equation (15) was used to experimentally determine the local permeability of both fluids. The bottom row in Fig. 6 shows the local permeability at the center of the microchannel, for 70.0% glycerol solution in water (left) and water (right). This one presents a monotonic increase with frequency, at small frequencies, a resonance at intermediate frequencies, and a monotonic decay with frequency at high frequencies. Our experimental results for the local dynamic permeability are also shown in a log-log scale in Fig. 3 for water (top) and 70.0% glycerol solution in water (bottom), with red dots. As this figure shows, experimental results are in agreement with the theoretical tendency of the model accounting for surface tension (continuous black line), in all the frequency range studied.

Our model, validated by experiments, allows us to understand the difference of several orders of magnitude in the amplitude of flow velocity at low frequencies, for systems with surface tension, when compared to classical single phase results (black line). We have shown results for two experiments for water pulsated at 1.0 Hz in Fig. 4. These are comparable with the black continuous line, which gives the theoretical result of our model.

For some of the experimental data we can observe different tendencies when the slug advances and when it recedes. This can be observed by visual inspection of the experimental data (red and cyan dots) around the first, third, and fifth maxima of Fig. 4 (corresponding to an advancing front), when compared to the second, fourth, and sixth maxima in the same figure (corresponding to a receding front). However, differences are within experimental error bars.

## IV. DISCUSSION

### A. Comparison between theory and experiment

#### 1. Glycerol

Figure 7 shows experimental and theoretical results for 70.0% glycerol solution in water. As error bars indicate, our dynamic permeabilities determined from experiments (in red) coincide with our theoretical model (black continuous line) and its associated errors (indicated with continuous dotted lines). The red dashed line indicates frequencies above which the linear approximation of the momentum equation is not expected to be valid (as explained below). For 70.0% glycerol solution in water, all experimental data fall below this line, so we can expect our theoretical model to coincide with experiments in all the frequency range studied. It is important to notice that, using a surface tension of 65.26 mN/m, reported in the literature, our model gives a value for resonance frequency of  $169.5 \pm 29.4$  Hz (indicated in the horizontal axis of Fig. 7) consistent with the one observed in experiments, in between 120.0 and 160.0 Hz.

#### 2. Water

Figure 8 shows experimental and theoretical data for water. As the error bars indicate, our dynamic permeabilities determined from experiments (in red) are consistent with theoretical results (black continuous line), at frequencies smaller than the resonance. Error bars for the theoretical curve are indicated with continuous dotted lines. The red dashed line indicates frequencies above which the linear approximation of the momentum equation is not expected to be valid and nonlinear terms would be needed to describe the dynamics. In this region, which is the region of the resonance, we do not expect quantitative agreement between the experimental dynamic permeability and the theoretical one. We have indicated in pink a vertical layer for the frequency range at which the theoretical permeability falls above the threshold (red dashed lines). Our theoretical prediction for the permeability in this frequency range is larger than the experimental results, suggesting that nonlinear terms in the momentum equation (which the actual physical system has) diminish the magnitude of the dynamic permeability at resonance. This is in agreement with convective

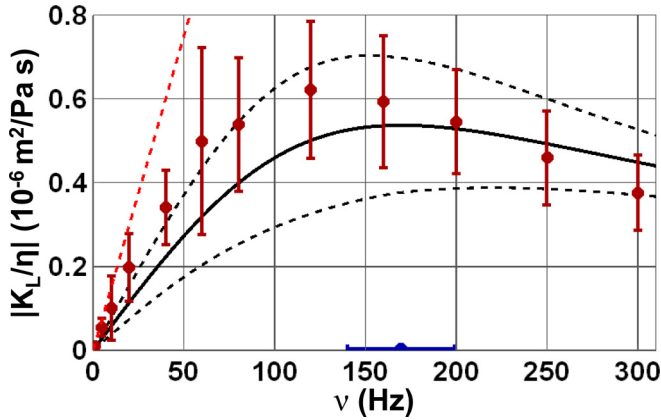


FIG. 7. Comparison between experimental and theoretical results for the dynamic permeability of a 70.0% glycerol solution in water slug containing two interfaces in a rectangular microchannel. For the figure, we have used the experimental parameters for 70.0% glycerol solution in water as in Fig. 3. Red circles: Experimental data. Black continuous line: Theoretical permeability, using a surface tension of 65.26 mN/m, reported in the literature [38]. Theoretical resonance is predicted at  $169.5 \pm 29.4$  Hz (blue dot in the frequency axis with an error bar). Black dashed line: Error bars for the theoretical permeability, accounting for uncertainty in slug length and channel dimensions. Red dashed line: Theoretical threshold above which the linear approximation is not valid.

terms creating dissipation and secondary flows [39,40]. For frequencies larger than the resonance frequency, theory and experiments should coincide. Experimental and theoretical error bars overlap at 250.0 Hz, above the resonance, where we also expect theory and experimental data to coincide; however, experimental results at 300.0 Hz are below the theoretical prediction. It is important to notice that, using a surface tension of 73.0 mN/m, reported in the literature, the linear model gives

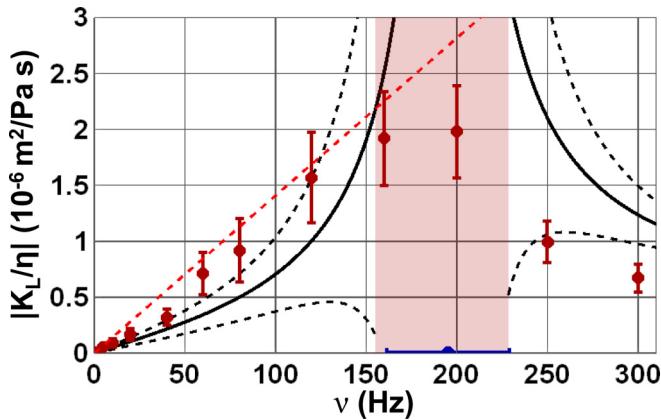


FIG. 8. Comparison between experimental and theoretical results for the dynamic permeability of a water slug containing two interfaces in a rectangular microchannel. Red circles: Experimental data. Black continuous line: Theoretical permeability, using a surface tension of 73.0 mN/m, reported in the literature. Theoretical resonance is predicted at  $195.2 \pm 33.8$  Hz (blue dot in the frequency axis with an error bar). Black dashed line: Error bars for the theoretical permeability, accounting for uncertainty in slug length and channel dimensions. Red dashed line: Theoretical threshold above which the linear approximation is not valid.

a value of resonance frequency of  $195.2 \pm 33.8$  Hz, consistent with the one observed in experiments, in between 160.0 and 200.0 Hz.

### 3. General features

As our experimental results for 70.0% glycerol solution in water and water show, the resonance is very close for both systems. This is due to the fact that the resonance frequency is independent of viscosity and the difference between both resonances comes through the factor  $\sqrt{\frac{\sigma}{\rho}}$  in the expression for  $\omega_{\text{res}}$  after Eq. (13). In the case of the two fluids studied here, this factor differs by only 15.0%, being larger for water. However the width of the resonance peak depends strongly on viscosity: the smaller the viscosity the sharper the resonance peak. We can distinctively see this when comparing the top and bottom panels of Fig. 3. We have also verified this theoretically for values of viscosities intermediate between the one of water and 70.0% glycerol solution in water.

#### B. Linearization of momentum equation

The validity of the linearized Navier-Stokes equations relies on the assumption of convective terms being negligible with respect to inertial terms. We could estimate the convective term as  $|\rho \mathbf{v} \cdot \nabla \mathbf{v}| \approx \frac{\rho v_{\text{max}}^2}{2l}$ , whereas the inertial term can be estimated as  $|\rho \frac{\partial v}{\partial t}| \approx \rho \omega v_{\text{max}}$ . This gives us a ratio

$$\frac{|\rho \mathbf{v} \cdot \nabla \mathbf{v}|}{|\rho \frac{\partial v}{\partial t}|} \approx \frac{v_{\text{max}}}{2l\omega}. \quad (17)$$

We consider that our linear model should give a good approximation whenever this ratio is below a certain threshold.

In the two figures analyzed in the previous section (Figs. 7 and 8), we have indicated with a red dashed line values of the permeability below which  $\frac{v_{\text{max}}}{2l\omega} < 0.15$ , where our theoretical model should be in agreement with experimental results.

#### C. Local vs global dynamic permeabilities

Figure 9 shows that in a range of frequencies, well above the linear regime, the local and the global permeabilities are related by a simple factor of  $3/2$ . This is an experimentally convenient feature of the solution, since it is much easier to track the interface position at the center of the channel than to track the interface profile in between the microchannel plates, which would represent focusing at different layers in between the plates, with a subsequent effort to reconstruct the profile in between the plates. The coincidence of both curves holds beyond the resonance frequency. Figure 9 (top) shows the agreement of these curves around resonance. Figure 9 (bottom) shows how the ratio of these curves is approximately one for frequencies around the resonance.

This feature allows us to accurately estimate the global dynamic permeability, which determines the magnitude of flow for a given pressure drop, from measurements of the front position in the middle of the channel.

#### D. Consistency with macroscopic experiments

An important remark is that for macroscopic systems for which  $L$  is very large, resonance would occur at extremely low frequencies that have not been studied in macroscopic experiments [19]. This resonance has to exist due to the presence of an interface. This can be appreciated analytically in Eq. (6).

Figure 10 shows (in red) data of the experimental local permeability reported in [19], together with the theoretical results of our model for the macroscopic dimensions used in that reference. For the figure, we have solved the problem in cylindrical coordinates, which was the geometry used in

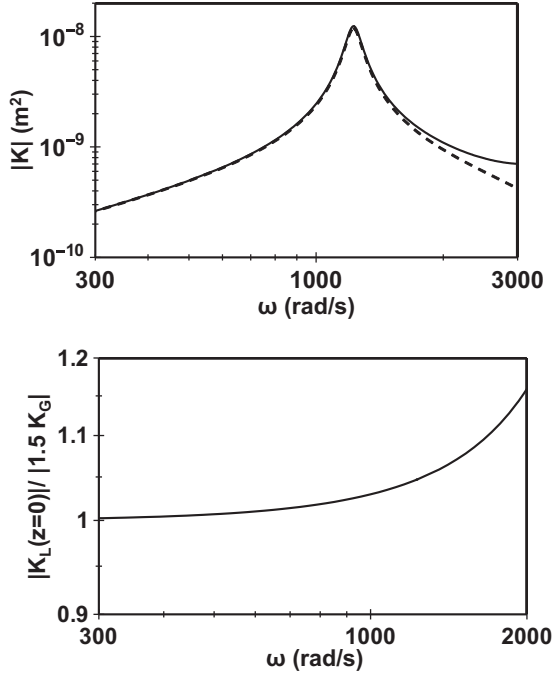


FIG. 9. Top: Comparison between theoretical local and global dynamic permeabilities for water around resonance. Global permeability has been rescaled by a factor of  $3/2$ . The coincidence of both curves goes beyond the linear regime observed in Fig. 3. Bottom: Ratio of both curves around resonance. Parameters are as in Fig. 3, top.

the macroscopic experiments, and have considered the presence of only one interface, since on one of the fluid-slug sides, there is a piston to move the fluid back and forth.

According to our model, theoretical resonance for this macroscopic system should happen at frequencies close to  $\omega_{\text{res}} \approx 0.96$  rad/s, which is much lower than the frequencies studied in the macroscopic experiment,  $\omega > 9$  rad/s. This is consistent with our statement that for frequencies much larger than  $\omega_{\text{res}}$ , the behavior of the local dynamic permeability is indistinguishable from the one of a single fluid.

Analogous to Eq. (16), the relation between Womersley and Laplace numbers, at resonance, is given by

$$\text{Wo}_{\text{res}}^2 = 2.4048 \sqrt{\frac{R}{L} \text{La}}, \quad (18)$$

where, for this cylindrical geometry,  $\omega_{\eta} = \frac{\eta}{\rho R^2}$  and  $\text{La} = 2\sigma \rho R / \eta^2$ ,  $R$  being the tube inner radius. From this expression it is clear that whenever  $\frac{R}{L} \text{La}$  is very small, the resonance frequency will be very small. The numerical factor 2.4048 comes from the first zero of a Bessel function,  $J_0$ , involved in the solution for this geometry.

Future macroscopic experiments, interested in phenomena at driving frequencies smaller than the resonance frequency, could benefit from taking into account that dynamic permeabilities in the presence of interfaces do not tend to the Hagen-Poiseuille limit, but decrease linearly toward zero, as the driving frequency approaches zero. For this purpose, the following expressions for the leading

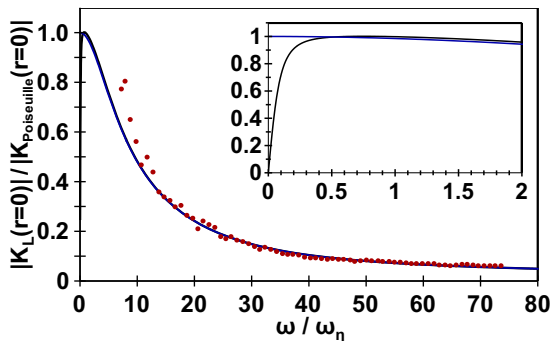


FIG. 10. Comparison between experimental and theoretical results for pure glycerol dynamic permeability reported by Castrejón Pita *et al.* [19] for a cylindrical geometry. Glycerol properties: Surface tension 63.4 mN/m, density 1250.0 kg/m<sup>3</sup>, viscosity 1.0 Pa s. Tube properties: Inner radius 25.0 mm, fluid column length 500.0 mm. The viscous frequency for this system is  $\omega_\eta = \frac{\eta}{\rho R^2} = 1.28$  rad/s. Inset figure, zoom at small frequencies. Red dots are experimental data taken from [19]. Blue curve is the single fluid theoretical local permeability; black curve is the local permeability in the presence of one fluid interface. The inset shows that resonance for this macroscopic system would happen at frequencies much lower than the ones that were studied in the macroscopic experiment.

order at small frequencies, of the local dynamic permeability, might be useful:

$$\frac{\text{Re}K_L}{\eta} = \frac{L^2 R^2 \eta}{16\sigma^2} \omega^2 \quad \text{and} \quad \frac{\text{Im}K_L}{\eta} = -\frac{LR^2}{8\sigma} \omega. \quad (19)$$

It is also worth mentioning that for the cylindrical geometry,  $|K_L| = 2|K_G|$ .

### E. Surface tension determination from experimental data

The leading term for the magnitude of the dynamic permeability at low frequencies gives, in principle, a way to determine surface tension. At leading order, the expansion of the modulus of the dynamic permeability at low frequencies is

$$\frac{|K_L|}{\eta} = \frac{L^2}{4\sigma} \omega. \quad (20)$$

Thus, if experimental data of  $\frac{|K_L|}{\eta}$  vs  $\omega$  at low frequencies were fitted to a straight line

$$\frac{|K_L|}{\eta} = m_{\text{fit}} \omega + b_{\text{fit}}, \quad (21)$$

we would obtain the fitting parameters  $m_{\text{fit}}$  and  $b_{\text{fit}}$ . We expect  $b_{\text{fit}}$  to have a value close to zero and can compute surface tension from the value of  $m_{\text{fit}}$  as

$$\sigma_{\text{fit}} = \frac{l^2 L}{4m_{\text{fit}}}. \quad (22)$$

Uncertainty in surface tension can be computed as

$$\delta\sigma_{\text{fit}} = \left| \frac{l^2}{4m_{\text{fit}}} \right| \delta L + \left| \frac{lL}{2m_{\text{fit}}} \right| \delta l + \left| \frac{l^2 L}{4m_{\text{fit}}^2} \right| \delta m_{\text{fit}}. \quad (23)$$

Here  $\delta m_{\text{fit}}$  can be obtained from the standard error of the slope  $m_{\text{fit}}$  in the linear regression done in Eq. (21).

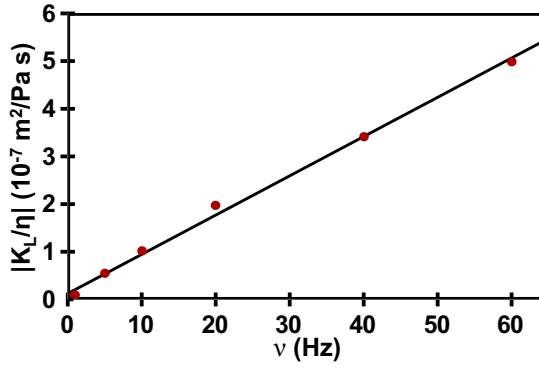


FIG. 11. Comparison between experimental data for 70.0% glycerol solution in water below 70.0 Hz (7 points) and a linear fit to the theoretical local dynamic permeability at small frequencies. The fitting leads to a surface tension value of  $45.8 \pm 17.1$  mN/m, with correlation  $R^2 = 0.996$ .

As a proof of concept, Fig. 11 illustrates that our experimental data exhibit a linear behavior at low frequencies. This one gives an estimated value of surface tension for 70.0% glycerol solution in water of  $45.8 \pm 17.1$  mN/m, in reasonable agreement with the value in the literature, namely,  $\sigma = 65.26$  mN/m.

Moreover, measuring resonance experimentally could as well allow one to have an indirect determination of surface tension, since from Eq. (13) we could write  $\sigma$  as

$$\sigma = \frac{2}{\pi^2} \rho l^2 L \omega_{\text{res}}. \quad (24)$$

In this case, we compute surface tension uncertainty as follows:

$$\delta\sigma_{\text{fit}} = \left| \frac{2}{\pi^2} \rho l^2 \omega_{\text{res}} \right| \delta L + \left| \frac{4}{\pi^2} \rho l L \omega_{\text{res}} \right| \delta l. \quad (25)$$

We obtain an estimated value of surface tension of  $\sigma = 58.2 \pm 20.2$  mN/m, again, consistent with the value in the literature.

The two measurements, together, could provide a way to test the consistency of the estimated value. Our error bars are not small, and we are not claiming validation of this method for surface tension determination. However, the consistency of our estimations with data in the literature suggests that an experiment specifically designed for that purpose could provide a way of experimentally determining surface tensions in microfluidics by means of pulsatile flows.

## F. Wetting

We have presented a theory for neutral wetting since we wanted to focus on the curvature created by the system as a response to external forcing. The natural curvature due to wetting between a fluid and a substrate is not caused by the pulsatile driving. Our model could also be used for hydrophilic or hydrophobic substrates with the following considerations.

We assume that the total curvature of the interface comes from two sources, wetting and forcing. For hydrophobic or hydrophilic surfaces, wetting is not neutral and curvatures due to wetting,  $\kappa_{\text{wetting}}^{1,2}$ , would have opposite signs at both sides of the fluid slug, as illustrated in the top panel of Fig. 12 for a hydrophilic case. In this situation, due to the Laplace condition, pressure in the fluid decreases by the same amount close to both interfaces, implying  $p_{\text{fluid}}^1 = p_{\text{air}}^1 - \sigma \kappa_{\text{wetting}}^1$  and  $p_{\text{fluid}}^2 = p_{\text{air}}^2 + \sigma \kappa_{\text{wetting}}^2 = p_{\text{air}}^2 - \sigma \kappa_{\text{wetting}}^1$ . This leads to cancellation of the curvature terms and to a pressure gradient equal inside and outside the fluid slug, that is,  $\Delta p_{\text{fluid}} = \Delta p_{\text{air}}$ . A similar analysis can be done for hydrophobic interactions, for which pressure in the fluid increases by the same



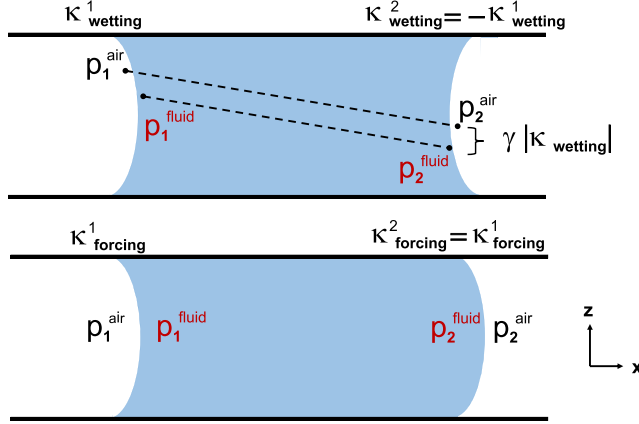


FIG. 12. Top: Illustration of pressure at the interfaces on both sides of the fluid slug for a hydrophilic surface. Curvature of the interface on the left,  $\kappa_{\text{wetting}}^1$ , and curvature of the interface at the right,  $\kappa_{\text{wetting}}^2$ , have opposite sign and approximately the same magnitude. Bottom: Illustration of pressure at the interfaces on both sides of the fluid slug forced periodically and neutral wetting, with instantaneous positive curvatures. Curvature of the interface on the left,  $\kappa_{\text{forcing}}^1$ , and curvature of the interface at the right,  $\kappa_{\text{forcing}}^2$ , have the same sign and approximately the same value.

amount close to both interfaces, leading to cancellation of the curvature terms and to a pressure gradient equal inside and outside the fluid slug.

Therefore, to a first approximation, the only contribution to pressure drop dynamics due to the Laplace condition would come from the curvature of interfaces as a response to the external periodic forcing. Since curvatures due to forcing,  $\kappa_{\text{forcing}}^{1,2}$ , would have the same sign in both interfaces, their effect will not cancel out. This is illustrated for neutral wetting, in the presence of forcing, in the bottom panel of Fig. 12, where an instantaneous curvature to the right is depicted. Since the driving is periodic, so will the curvature be, sometimes in phase with the forcing, sometimes out of phase with it, depending on the driving frequency.

As a result of our assumption,

$$\Delta p_{\text{fluid}} = \Delta p_{\text{air}} + \sigma \kappa_{\text{forcing}}^1 + \sigma \kappa_{\text{forcing}}^2, \quad (26)$$

which is equal to Eq. (2) used to construct the model.

Under this approximation, velocity is independent of wetting and our results for velocity and permeabilities remain identical. Only the interface shapes  $u_1$  and  $u_2$  could be different. Once the velocity is known, Eq. (4) could be integrated with an initial condition for the shape of each interface. This initial condition could take into account the static contact angle [41]. The dynamic contact angle would then be determined from the instantaneous slope of interface position at the wall.

Moreover, approximating interfacial curvatures as concavities of the interface position, according to

$$\kappa = -\frac{\frac{\partial^2 u}{\partial z^2}}{\left[1 + \left(\frac{\partial u}{\partial z}\right)^2\right]^{3/2}} \approx -\frac{\partial^2 u}{\partial z^2}, \quad (27)$$

is appropriate for hydrophobic or hydrophilic interactions close to neutral wetting, since the factor  $1/[1 + (\frac{\partial u}{\partial z})^2]^{3/2}$  is close to unit. For the experiments presented here, the largest deviation from the actual curvature and the approximated curvature happened for water at resonance, where the factor  $1/[1 + (\frac{\partial u}{\partial z})^2]^{3/2} \approx 0.83$ , which did not give a significant change to theoretical curves (not shown).

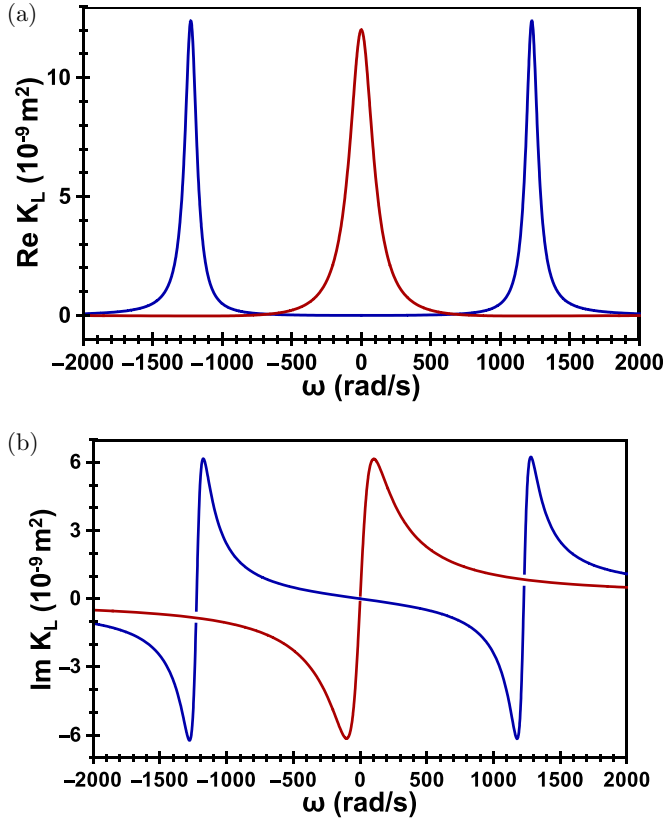


FIG. 13. Local dynamic permeabilities, at the center of the channel, illustrating the singular nature of surface tension at low frequencies, for zero surface tension (red lines) and air-water surface tension (blue lines). (a) Real parts; (b) imaginary parts.

### G. Singular character of surface tension

Equation (5) shows how the presence of surface tension changes the nature of the dynamic equation, when compared to the equation that describes a single fluid. In the presence of surface tension, we have an integro-differential equation for the fluid velocity in the time domain, while for a single fluid we have a differential equation, without the last term in Eq. (5). In the frequency domain, Eq. (6) shows how surface tension modifies the nature of the coefficient multiplying the highest order derivative in the equation. For any finite value of surface tension, the imaginary part of the coefficient multiplying  $\frac{\partial^2 \hat{v}}{\partial z^2}$  tends to infinity when  $\omega$  tends to zero. As in many other systems, from which the best known example in fluids is the Saffman-Taylor problem [42], surface tension changes the mathematical nature of a problem [43–45], in this case, the low-frequency behavior of the permeability. Figure 13 illustrates, through the real and imaginary parts of the dynamic permeability, the singular character of surface tension.

For a finite surface tension, the leading terms in the zero-frequency limit of the real and imaginary parts of the local permeability, at the center of the channel, are given by  $\frac{\text{Re}K_L}{\eta} = \frac{L^2 l^2 \eta}{8\sigma^2} \omega^2$  and  $\frac{\text{Im}K_L}{\eta} = -\frac{Ll^2}{4\sigma} \omega$ . This is in clear contrast to the corresponding limit, in the absence of surface tension, for which, at leading order, the real part of the permeability is a constant, equal to  $\frac{\text{Re}K_L}{\eta} = \frac{l^2}{2\eta}$ , and the imaginary part is linear in frequency, but with a positive slope, that is,  $\frac{\text{Im}K_L}{\eta} = \frac{5\rho l^4}{24\eta^2} \omega$ . These features can be qualitatively appreciated in Fig. 13.

## V. LIMITATIONS

In our model we have considered a solution for parallel plates, where the microchannel thickness,  $2\ell$ , is considered to be much smaller than any other dimension in the system, so that the effect of lateral walls can be neglected. Our experimental setting has a rectangular microchannel with a cross-section aspect ratio equal to 3.23. An approximated correction to account for the rectangular channel can be computed following Tabeling [46], that for a single fluid, and our channel dimensions, implies a 1.3% difference in flow velocity at the center of the microchannel. Another possible source of uncertainty is the microchannel roughening [47,48], which we have not accounted for or quantified.

## VI. CONCLUSIONS

We have presented a simple theoretical model to study how the presence of air-fluid interfaces affects the dynamics of a fluid confined at microscales. Our model incorporates dynamic interfacial curvatures produced as a response to pulsatile external forcing. We have also designed and implemented microfluidic experiments and obtained the experimental dynamic permeability for water and a 70.0% glycerol solution in water. We observed an agreement with our theoretical predictions.

Our model, validated by experiments, has allowed us to understand differences of several orders of magnitude in the amplitude of flow velocity at low frequencies, between systems with and without air-fluid interfaces. We have discussed in length the different experimental and theoretical aspects of our findings including a proposal to measure surface tension in microfluidics via pulsatile forcing. We have found that the presence of surface tension confers a radically different behavior to the dynamic permeability, not only when compared with the one of a single fluid, but when compared to the one of any other system reported in the literature, including those having elastic features, for which a permeability tending to zero in the limit of zero frequency has not been reported.

The coupled effect of interfaces and pulsatile forcing allows for controlling the magnitude of flow velocity in a wide range of values by simply changing the frequency of the piezoactuator. This could be potentially exploited in organ-on-a-chip devices to tune the physiological mechanical conditions of the cells, or to study how cells would respond to different imposed, nonphysiological stresses.

## ACKNOWLEDGMENTS

The authors thank J. Lombard and G. Caballero for useful discussions. P.V.V. thanks CONA-CyT (Mexico) for two-year postdoctoral funding through Project No. 219584. U.T. and E.C.P. acknowledge financial support from CONACyT (Mexico) through Project No. 219584. The authors acknowledge financial support from the Faculty of Chemistry, UNAM, through PAIP Projects No. 5000-9011 and No. 5000-9023.

## APPENDIX A: EXPERIMENTAL SETUP

The experimental setup is illustrated in Fig. 1. It consists of an oscillation generator connected to a microfluidic channel, a differential pressure sensor, and a high-speed camera. The microfluidic channel measures  $37.480 \pm 0.105$  mm long,  $1.001 \pm 0.041$  mm wide, and  $0.310 \pm 0.046$  mm deep and was constructed in PMMA. A volume of the fluid under study (approximately  $3.0 \mu\text{L}$ ) was confined in the middle, creating two air-liquid interfaces: the interface facing the oscillation generator *IF1*, and the interface near the exit open to the atmosphere *IF2* (Fig. 1). The distance between both interfaces was 1.0 cm. The microfluidic channel has four openings. The first one (piezoactuator input in Fig. 1) serves as a connection site between the oscillation generator and the microchannel by means of a PTFE tubing of 0.508 mm inner diameter (ID), 1.19 mm outer diameter (OD), and 1.0 cm long (Microbore PTFE Tubing, Cole-Parmer). The second and third openings (*pressure sensor* labeled in Fig. 1) are the differential pressure sensor measuring sites, which are attached, with the same type of PTFE tubing, to a Honeywell pressure sensor (Honeywell

142PC01G). The last opening is the outlet facing the atmosphere. The oscillation generator is made of a polypropylene rigid tube (marked with a small dashed-line rectangle beside the elastic membrane in Fig. 1) 1.5 cm long and 4.7 mm diameter, covered with an elastic membrane adhered to a piezoelectric actuator (APF705, Thorlabs) by means of an acrylic cylinder. This arrangement creates a chamber sealed with a plunger at one of its ends. On the other side, a PTFE tubing (1.19 mm ID, 1.69 mm OD, 10.0 cm long, Microbore PTFE Tubing, Cole-Parmer) connects the chamber with the tubing of the first microchannel entrance. The tensile strength of the PTFE tubing is approximately 17 MPa, high enough to consider it as a rigid tube relative to the pressure range used in our experiments (approximately 200.0 Pa).

The piezoelectric generates vibrations of adjustable amplitude and frequency that are transferred to the air. This one moves the fluid slug back and forth. We monitor the pressure difference in the air, at both sides of the fluid slug. To control the piezoelectric movement we use a multifunction data acquisition device (USB-6351, National Instruments) that generates a sinusoidal electrical signal at specific frequencies and voltages (0.75–1.5 V peak-to-peak). This signal is magnified 100-fold by a Trek PZD350A high-voltage amplifier (bandwidth: 250.0 kHz for large signal) and then sent to the piezoelectric. The multifunctional device also records the exact pressure changes detected by the pressure sensor every 0.2 ms, which is the shortest response time of the pressure sensor. The pressure signal is fitted to a sine function to suppress high frequencies, associated with sensor resolution and electric noise. This information is used for tuning the voltage in such a way that the amplitude of the pressure drop driving the interface is kept approximately constant for all frequencies. We track the interface position as a function of time,  $U(t)$ , on the slug side farther from the piezoelectric ( $IF2$ ). The position of the interface was recorded at the mid-height of the channel using bright-field microscopy with a 10 $\times$  objective (Leica HI PLAN I, NA = 0.22, depth of field = 12.2  $\mu\text{m}$  calculated with a wavelength of 550.0 nm) using a Phantom Miro M110 (Vision Research) high-speed camera coupled to an inverted microscope (DM IL LED, Leica). All images had a spatial resolution of 1.9  $\mu\text{m}$  per pixel, determined with a stage micrometer (Pysen-SGI). The sampling frequency of the videos was adjusted for each pulsatile forcing frequency, in such a way that there were at least 10 and up to 50 frames per cycle (30.0 to 3000.0 fps). The shutter speed was modified for each video as  $1/(2 \times \text{fps})$ . The interface was recorded after a 10.0 second stabilization period and the size of the fluid slug was verified after each measurement to confirm that no appreciable evaporation had occurred; otherwise, the channel was emptied and a new recording was made with a 1.0-cm-long fresh slug.

We made experiments with two model fluids: filtrated, deionized water (Milli-Q) and a freshly prepared 70.0% (v/v) glycerol solution in water (filtrated and deionized).

## APPENDIX B: MICROFABRICATION

To build the microfluidic device, we drilled a straight microchannel in a 2.0-mm-thick PMMA wafer using a CNC engraving machine (CNC3018) equipped with a 0.8 mm two-flute carbide end mill (see Appendix A for exact measurements). A second PMMA wafer of the same thickness with four-drilled openings (Fig. 1) was bonded to seal the microchannel as follows. The wafers were thoroughly cleaned and exposed to volatilized chloroform for 4.0 min. Afterwards, they were pressed together by hand (1.0 min) [49], and then pressed by a pair of slides and clamps. Finally, they were sonicated in ethanol at 50  $^{\circ}\text{C}$  for 15.0 minutes [50–52]. This method is effective as it provides a high bonding strength (0.95 MPa) and the microchannel dimensions change very little due to the process (0.3%–0.8%) [50].

## APPENDIX C: MEAN AND ERROR BARS OF COMBINED EXPERIMENTS

In this Appendix we present detailed information of how mean and error bars of data for pressure, position, velocity and permeabilities were obtained.

The pressure drop recordings were acquired at a sampling frequency of 5000.0 data per second. The pressure drop signals were fitted to a sinusoidal function using

$$\Delta p_k^{\text{fit}}(t) = \Delta p_k \sin(2\pi \nu t + \phi_k), \quad (\text{C1})$$

where  $\Delta p_k$  is the amplitude of the fit of the  $k$  experiment,  $\nu$  the driving frequency, and  $\phi_k$  the phase shift. Each fitted data  $\Delta p_i^{\text{fit}}$  and experimental data  $\Delta p_i^{\text{exp}}$  around the maxima and minima, located at the same time instant,  $i$ , and the total number of these pairs  $n_k$ , for experiment  $k$ , were then used in Eq. (C2) for error bar calculation of maxima (minima):

$$s_k = \sqrt{\frac{\sum_{i=1}^{n_k} (\Delta p_k^{i-\text{exp}} - \Delta p_k^{i-\text{fit}})^2}{n_k}}. \quad (\text{C2})$$

The mean of all  $j$  experiments was calculated as

$$\Delta p_{\text{air}}^o = \sum_{k=1}^j \frac{\Delta p_k}{j}, \quad (\text{C3})$$

where  $j$  is the total number of experiments, generally  $j = 4$ . The error bars of all combined experiments were calculated using Eq. (C4):

$$\delta \Delta p_{\text{air}}^o = \sqrt{\frac{\sum_{k=1}^{2j} (n_k - 1) s_k^2}{\sum_{k=1}^{2j} n_k - 2j}}. \quad (\text{C4})$$

The superscript  $2j$  is due to the fact that we have computed uncertainties in a separate way for maxima and minima of the  $j$  experiments.

Amplitude of the interface position in time was obtained by image analysis using Matlab. The maxima of all cycles were averaged as

$$H_k^{\text{max}} = \sum_{i=1}^{n_k} \frac{|h_i^{\text{max}}|}{n_k}, \quad (\text{C5})$$

where  $n_k$  is the total number of maxima of experiment  $k$ ; from this data the standard deviation  $s_{\text{max},k}$  of each experiment was obtained from data dispersion, and the same was done for minima. The mean position was calculated as

$$H_{\text{mean}} = \sum_{k=1}^j \frac{|H_k^{\text{max}}| + |H_k^{\text{min}}|}{2j}. \quad (\text{C6})$$

The error bars of the combined experiments are calculated using the following expression:

$$\delta H = \sqrt{\frac{\sum_{k=1}^j (n_k - 1) (s_{\text{max},k}^2 + s_{\text{min},k}^2)}{2(\sum_{k=1}^j n_k - j)}}}, \quad (\text{C7})$$

where  $n_k$  is the number of cycles averaged for each experiment.

The velocity amplitude for each experiment was obtained by numerical differentiation in time of the smoothed position data. The maxima of all cycles were averaged as

$$V_k^{\text{max}} = \sum_{i=1}^{n_k} \frac{|v_i^{\text{max}}|}{n_k}, \quad (\text{C8})$$

where  $n_k$  is the total number of maxima of experiment  $k$ , the standard deviation  $s_{\text{max},k}$  of each experiment was obtained from data dispersion, and the same was done for minima. The mean velocity was calculated as

$$v_{\text{max}} = \sum_{k=1}^j \frac{|V_k^{\text{max}}| + |V_k^{\text{min}}|}{2j}. \quad (\text{C9})$$

The error bars were calculated using the following expression:

$$\delta V = \sqrt{\frac{\sum_{k=1}^j (n_k - 1)(s_{\max,k}^2 + s_{\min,k}^2)}{2(\sum_{k=1}^j n_k - j)}}, \quad (C10)$$

where  $n_k$  is the number of cycles averaged and  $s_{\max,k}$  ( $s_{\min,k}$ ) is the standard deviation of the maxima (minima) of the  $k$ th experiment.

The modulus of the dynamic permeability was calculated using Eq. (15), independently for maxima and minima, according to

$$\frac{K_k^{\max}}{\eta} = \frac{V_k^{\max}}{\Delta p_{\text{air}}^o} L. \quad (C11)$$

The same was done for minima. The mean modulus of dynamic permeability of all  $k$  experiments was calculated as

$$\frac{K_L}{\eta} = \sum_{k=1}^j \frac{1}{2j} \left( \frac{K_k^{\max}}{\eta} + \frac{K_k^{\min}}{\eta} \right), \quad (C12)$$

consistent with analyzing independently minima and maxima in Eq. (C9).

As the dynamic permeability depends on three variables, the error  $\delta \frac{K_k^{\max}}{\eta}$  of each experiment was calculated using the following expression:

$$\delta \frac{K_k^{\max}}{\eta} = \frac{L}{\Delta p_{\text{air}}^o} \delta V_k^{\max} + \frac{V_k^{\max} L}{(\Delta p_{\text{air}}^o)^2} \delta \Delta p_{\text{air}}^o + \frac{V_k^{\max}}{\Delta p_{\text{air}}^o} \delta L. \quad (C13)$$

The same was done for  $\delta \frac{K_k^{\min}}{\eta}$ . Error bars of all  $j$  experiments combined were calculated using the following expression:

$$\delta \frac{K_L}{\eta} = \sqrt{\sum_{k=1}^j \frac{1}{2j} \left[ \left( \delta \frac{K_k^{\max}}{\eta} \right)^2 + \left( \delta \frac{K_k^{\min}}{\eta} \right)^2 \right]}. \quad (C14)$$

- 
- [1] Y. Xie, C. Chindam, N. Nama *et al.*, Exploring bubble oscillation and mass transfer enhancement in acoustic-assisted liquid-liquid extraction with a microfluidic device, *Sci. Rep.* **5**, 12572 (2015).
  - [2] G. Lestari, A. Salari, M. Abolhasani and E. Kumacheva, A microfluidic study of liquid-liquid extraction mediated by carbon dioxide, *Lab Chip* **16**, 2710 (2016).
  - [3] P. Tabeling, M. Chabert, A. Dodge *et al.*, Chaotic mixing in cross-channel micromixers, *Philos. Trans. R. Soc., A* **362**, 987 (2004).
  - [4] B. Wang, J. L. Xu, W. Zhang, and Y. X. Li, A new bubble-driven pulse pressure actuator for micromixing enhancement, *Sens. Actuators, A* **169**, 194 (2011).
  - [5] M. Alizadehgiashi, A. Khabibullin, Y. Li *et al.*, Shear-induced alignment of anisotropic nanoparticles in a single-droplet oscillatory microfluidic platform, *Langmuir* **34**, 322 (2018).
  - [6] K. Jo, Y.-L. Chen, J. J. de Pablo, and D. C. Schwartz, Elongation and migration of single DNA molecules in microchannels using oscillatory shear flows, *Lab Chip* **9**, 2348 (2009).
  - [7] G. Whitesides, The origins and the future of microfluidics, *Nature (London)* **442**, 368 (2016).
  - [8] M. Abolhasani and K. F. Jensen, Oscillatory multiphase flow strategy for chemistry and biology, *Lab Chip* **16**, 2775 (2016).
  - [9] C. N. Baroud, F. Gallaire, and R. Dangla, Dynamics of microfluidic droplets, *Lab Chip* **10**, 2032 (2010).
  - [10] P. A. Basilio, A. M. Torres Rojas, E. Corvera Poiré, and L. F. Olguín, Stream of droplets as an actuator for oscillatory flows in microfluidics, *Microfluid. Nanofluid.* **23**, 64 (2019).

- [11] M. Y. Zhou and P. Sheng, First-principles calculations of dynamic permeability in porous media, *Phys. Rev. B* **39**, 12027 (1989).
- [12] M. Castro, M. E. Bravo-Gutiérrez, A. Hernández-Machado, and E. Corvera Poiré, Dynamic Characterization of Permeabilities and Flows in Microchannels, *Phys. Rev. Lett.* **101**, 224501 (2008).
- [13] R. Collepardo-Guevara and E. Corvera Poiré, Controlling viscoelastic flow by tuning frequency during occlusions, *Phys. Rev. E* **76**, 026301 (2007).
- [14] M. E. Bravo-Gutiérrez, M. Castro, A. Hernández-Machado, and E. Corvera Poiré, Controlling viscoelastic flow in microchannels with slip, *Langmuir* **27**, 2075 (2011).
- [15] M. López de Haro, J. A. del Río, and S. Whitaker, Flow of maxwell fluids in porous media, *Transp. Porous Media* **25**, 167 (1996).
- [16] J. A. del Río, M. L. de Haro, and S. Whitaker, Enhancement in the dynamic response of a viscoelastic fluid flowing in a tube, *Phys. Rev. E* **58**, 6323 (1998).
- [17] E. Corvera Poiré and A. Hernández-Machado, Frequency-induced stratification in viscoelastic microfluidics, *Langmuir* **26**, 15084 (2010).
- [18] A. M. Torres Rojas and E. Corvera Poiré, Cooperation and competition of viscoelastic fluids and elastomeric microtubes subject to pulsatile forcing, *Phys. Rev. Fluids* **5**, 063303 (2020).
- [19] J. R. Castrejón-Pita, J. A. del Río, A. A. Castrejón-Pita, and G. Huelsz, Experimental observation of dramatic differences in the dynamic response of Newtonian and Maxwellian fluids, *Phys. Rev. E* **68**, 046301 (2003).
- [20] M. Torralba, J. R. Castrejón-Pita, A. A. Castrejón-Pita, G. Huelsz, J. A. del Río, and J. Ortin, Measurements of the bulk and interfacial velocity profiles in oscillating Newtonian and Maxwellian fluids, *Phys. Rev. E* **72**, 016308 (2005).
- [21] D. Tsiklauri and I. Beresnev, Enhancement in the dynamic response of a viscoelastic fluid flowing through a longitudinally vibrating tube, *Phys. Rev. E* **63**, 046304 (2001).
- [22] A. M. Torres Rojas, I. Pagonabarraga, and E. Corvera Poiré, Resonances of Newtonian fluids in elastomeric microtubes, *Phys. Fluids* **29**, 122003 (2017).
- [23] D. C. Leslie, C. J. Easley, E. Seker, J. M. Karlinsey, M. Utz, M. R. Begley, and J. P. Landers, Frequency-specific flow control in microfluidic circuits with passive elastomeric features, *Nat. Phys.* **5**, 231 (2009).
- [24] D. Yáñez, R. D. M. Travasso, and E. Corvera Poiré, Resonances in the response of fluidic networks inherent to the cooperation between elasticity and bifurcations, *R. Soc. Open Sci.* **6**, 190661 (2019).
- [25] J. Lombard, I. Pagonabarraga, and E. Corvera Poiré, Dynamic permeability of a compressible binary fluid mixture, *Phys. Rev. Fluids* **5**, 064201 (2020).
- [26] J. Flores, E. Corvera Poiré, J. A. del Río, and M. López de Haro, A plausible explanation for heart rates in mammals, *J. Theor. Biol.* **265**, 599 (2010).
- [27] K. L. Pitts and M. Fenech, Micro-particle image velocimetry for velocity profile measurements of micro blood flows, *JoVE* **74**, e50314 (2013).
- [28] S. T. Wereley and C. D. Meinhart, Micron-resolution particle image velocimetry, in *Microscale Diagnostic Techniques* (Springer, Berlin, Heidelberg, 2005), pp. 51–112.
- [29] A. Melling, Tracer particles and seeding for particle image velocimetry, *Meas. Sci. Technol.* **8**, 1406 (1997).
- [30] D. Huh, A human breathing lung-on-a-chip, *Ann. Am. Thorac. Soc.* **12**(Suppl. 1), S42 (2015).
- [31] J. Atencia and D. J. Beebe, Controlled microfluidic interfaces, *Nature (London)* **437**, 648 (2005).
- [32] D. R. Reyes, D. Iossifidis, P. A. Auroux, and A. Manz, Micro total analysis systems. 1. Introduction, theory, and technology, *Anal. Chem.* **74**, 2623 (2002).
- [33] H. A. Stone, A. D. Stroock, and A. Ajdari, Engineering flows in small devices: Microfluidics toward a laboratory-on-a-chip, *Annu. Rev. Fluid Mech.* **36**, 381 (2004).
- [34] G. Dai, M. R. Kaazempur-Mofrad, S. Natarajan, Y. Zhang, S. Vaughn, B. R. Blackman, R. D. Kamm, G. García-Cardena, and M. A. Gimbrone, Jr., Distinct endothelial phenotypes evoked by arterial waveforms derived from atherosclerosis-susceptible and -resistant regions of human vasculature, *Proc. Natl. Acad. Sci. USA* **101**, 14871 (2004).
- [35] D. B. Weibel and G. M. Whitesides, Applications of microfluidics in chemical biology, *Curr. Opin. Chem. Bio.* **10**, 584 (2006).



- [36] D. R. Meldrum and M. R. Holl, Microscale bioanalytical systems, *Science* **297**, 1197 (2002).
- [37] Our formalism could serve equally well when there is only one air-fluid interface and a solid-fluid boundary, as when the fluid is in contact with a piston, for instance, in the macroscopic experiments for Newtonian fluids [19]. In this case, we would have only one of the terms  $\sigma\kappa$ .
- [38] *Physical Properties of Glycerine and Its Solutions* (Glycerine Producers Association, 1963).
- [39] G. R. Wang, F. Yang, and W. Zhao, There can be turbulence in microfluidics at low Reynolds number, *Lab Chip* **14**, 1452 (2014).
- [40] Z. Wu, N. T. Nguyen, and X. Huang, Nonlinear diffusive mixing in microchannels: Theory and experiments, *J. Micromech. Microeng.* **14**, 604 (2004).
- [41] T. S. Meiron, A. Marmur, and S. Sam, Contact angle measurement on rough surfaces, *J. Colloid Interface Sci.* **274**, 637 (2004).
- [42] P. G. Saffman and G. I. Taylor, The penetration of a fluid into a porous medium or Hele-Shaw cell containing a more viscous liquid, *Proc. R. Soc. Ser. A Math. Phys. Sci.* **245**, 312 (1958).
- [43] B. I. Shraiman, Velocity Selection and the Saffman-Taylor Problem, *Phys. Rev. Lett.* **56**, 2028 (1986).
- [44] D. C. Hong and J. S. Langer, Analytic Theory of the Selection Mechanism in the Saffman-Taylor Problem, *Phys. Rev. Lett.* **56**, 2032 (1986).
- [45] R. Combescot, T. Dombre, V. Hakim, Y. Pomeau, and A. Pumir, Shape Selection of Saffman-Taylor Fingers, *Phys. Rev. Lett.* **56**, 2036 (1986).
- [46] P. Tabeling, *Introduction to Microfluidics* (Oxford University Press, Oxford, England, 2006).
- [47] S. Bakhshian, M. Murakami, S. A. Hosseini, and Q. Kang, Scaling of imbibition front dynamics in heterogeneous porous media, *Geophys. Res. Lett.* **47**, e2020GL087914 (2020).
- [48] M. Queralt-Martín, M. Pradas, R. Rodríguez-Trujillo, M. Arundell, E. Corvera Poiré, and A. Hernández-Machado, Pinning and Avalanches in Hydrophobic Microchannels, *Phys. Rev. Lett.* **106**, 194501 (2011).
- [49] I. R. G. Ogilvie, V. J. Sieben, C. F. A. Floquet, R. Zmijan, M. C. Mowlem, and H. Morgan, Reduction of surface roughness for optical quality microfluidic devices in PMMA and COC, *J. Micromech. Microeng.* **20**, 065016 (2010).
- [50] Z. Zhang, X. Wang, Y. Luo, S. He, and L. Wang, Thermal assisted ultrasonic bonding method for poly(methyl methacrylate) (PMMA) microfluidic devices, *Talanta* **81**, 1331 (2010).
- [51] A. Bamshad, A. Nikfarjam, and H. Khaleghi, A new simple and fast thermally-solvent assisted method to bond PMMA-PMMA in micro-fluidics devices, *J. Micromech. Microeng.* **26**, 065017 (2016).
- [52] S. W. Li, J. H. Xu, Y. J. Wang, Y. C. Lu, and G. S. Luo, Low-temperature bonding of poly-(methyl methacrylate) microfluidic devices under an ultrasonic field, *J. Micromech. Microeng.* **19**, 015035 (2008).